

Disturbed Flow-Facilitated Margination and Targeting of Nanodisks Protect against Atherosclerosis

Chuan-Rong Zhao, Jingyi Li, Zhi-Tong Jiang, Juan-Juan Zhu, Jia-Nan Zhao, Qian-Ru Yang, Weijuan Yao, Wei Pang, Ning Li, Miaorong Yu,* Yong Gan,* and Jing Zhou*

Disturbed blood flow induces endothelial pro-inflammatory responses that promote atherogenesis. Nanoparticle-based therapeutics aimed at treating endothelial inflammation in vasculature where disturbed flow occurs may provide a promising avenue to prevent atherosclerosis. By using a vertical-step flow apparatus and a microfluidic chip of vascular stenosis, herein, it is found that the disk-shaped versus the spherical nanoparticles exhibit preferential margination (localization and adhesion) to the regions with the pro-atherogenic disturbed flow. By employing a mouse model of carotid partial ligation, superior targeting and higher accumulation of the disk-shaped particles are also demonstrated within disturbed flow areas than that of the spherical particles. In hyperlipidemia mice, administration of disk-shaped particles loaded with hypomethylating agent decitabine (DAC) displays greater anti-inflammatory and anti-atherosclerotic effects compared with that of the spherical counterparts and exhibits reduced toxicity than “naked” DAC. The findings suggest that shaping nanoparticles to disk is an effective strategy for promoting their delivery to atheroprone endothelia.

suggests a pivotal role of local hemodynamic shear stress in atherogenesis.^[2] Disturbed blood flow with low and reciprocating shear stress in arterial branches and curvatures induces the expression of pro-inflammatory molecules in vascular endothelial cells (ECs) lining the inner surface of the vasculature, and hence, promotes infiltration of circulating monocytes through the damaged endothelia into the arterial wall, as well as migration of smooth muscle cells into the subintimal space, initiating atherogenesis.^[3] In contrast, laminar flow with a clear shear direction and high shear rate in the straight parts of the arteries is atheroprotective.^[4] Thus, targeting the atheroprone pro-inflammatory endothelia has emerged as a potential therapeutic strategy against atherosclerosis.^[5] However, the low delivery efficiency, lack of targeting capability, and off-target effects of current anti-inflammation

therapies have contributed to the challenges in cardiovascular drug discovery and development.^[6,7]

Nanoparticle-based drug delivery systems have the capability to improve local treatment for preventing off-target organ

1. Introduction


Atherosclerotic cardiovascular diseases remain the leading causes of death worldwide.^[1] The focal nature of atherosclerosis

C.-R. Zhao, Z.-T. Jiang, J.-J. Zhu, J.-N. Zhao, Q.-R. Yang, W. Yao, W. Pang, J. Zhou

Department of Physiology and Pathophysiology
School of Basic Medical Sciences
Hemorheology Center
School of Basic Medical Sciences
Peking University
Beijing 100191, China
E-mail: jzhou@bjmu.edu.cn

C.-R. Zhao, Z.-T. Jiang, J.-J. Zhu, J.-N. Zhao, Q.-R. Yang, J. Zhou
Key Laboratory of Molecular Cardiovascular Science
Ministry of Education
Beijing 100191, China

C.-R. Zhao, Z.-T. Jiang, J.-J. Zhu, J.-N. Zhao, Q.-R. Yang, J. Zhou
National Health Commission Key Laboratory of Cardiovascular
Molecular Biology and Regulatory Peptides
Beijing Key Laboratory of Cardiovascular Receptors Research
Peking University
Beijing 100191, China

 The ORCID identification number(s) for the author(s) of this article can be found under <https://doi.org/10.1002/smll.202204694>.

J. Li, M. Yu, Y. Gan
State Key Laboratory of Drug Research
Shanghai Institute of Materia Medica
Chinese Academy of Sciences
Shanghai 201203, China
E-mail: mryu@simm.ac.cn; ygan@simm.ac.cn

Z.-T. Jiang
Department of Cardiovascular Surgery
Peking University Shenzhen Hospital
Shenzhen 518036, China

N. Li
Center for Biomechanics and Bioengineering
Key Laboratory of Microgravity (National Microgravity Laboratory), and
Beijing Key Laboratory of Engineered Construction and Mechanobiology
Institute of Mechanics
Chinese Academy of Sciences
Beijing 100190, China

N. Li
School of Engineering Sciences
University of Chinese Academy of Sciences
Beijing 100049, China

M. Yu, Y. Gan
University of Chinese Academy of Sciences
Beijing 100049, China

DOI: 10.1002/smll.202204694

toxicity in treating atherosclerosis.^[8–10] Their tunable shape, size, and surface chemistry enable them to be engineered for site-specific delivery.^[11] Among the above parameters, it has been recognized that shape may modulate particle circulation, bio-distribution, and cellular internalization.^[12,13] For instance, due to their rotational motion in shear flow, non-spherical particles (e.g., spheroids, ellipsoids, rods, and disks) can undergo superior margination (i.e., lateral drift) than spheres in the presence or absence of external forces, and thereby, achieve enhanced localization and adhesion.^[14–16] Disk-shaped nanoparticles have exhibited improved margination under different physiologically relevant laminar flow and superior cellular uptake in an experimental static condition compared with spherical and/or rod-like counterparts.^[17–19] Although there was few *in vivo* evidence echoing the differences in particle margination, disk-shaped platelets naturally accumulate to downstream of narrowed blood vessels, the post-stenotic area where flow disturbance occurs, hinting at their special targeting ability.^[20] A recent ingeniously designed study using a microfluidic model of vascular stenosis has demonstrated rapid margination of nanoparticles in the post-stenotic disturbed flow area.^[21] These findings strongly inform us that shape may contribute to elevated targeting of particles to disturbed flow-activated atheroprone endothelia. The correlation between the shape of nanoparticles and their margination in disturbed versus laminar flow conditions *in vivo*, however, remains unexplored, even though this aspect is potentially crucial in the applications of nanotherapeutics.

Our prior studies have shown that 5-Aza-2'-deoxycytidine (decitabine, DAC) has an anti-inflammation activity in vascular endothelium through inhibiting the disturbed flow-induced endothelial DNA hypermethylation via depleting the epigenetic regulator DNA methyltransferase 1 (DNMT1).^[22,23] Intraperitoneal injection of DAC in apolipoprotein E-deficient (ApoE^{-/-}) mice inhibited atheroma formation in the disturbed flow areas.^[24] DAC has been approved by the U.S. Food and Drug Administration for application as a monotherapeutic agent against hematological malignancies,^[25] but has not yet been used in clinical practice to treat or prevent atherosclerosis. The major disadvantages of DAC for future application in cardiovascular disease are its instability both *in vitro* and *in vivo* and the effects of inhibiting bone marrow hematopoiesis and damaging the nervous system.^[26–28] DAC-loaded nanoparticles have been constructed and applied for the treatment of various cancers and bone marrow disorders-related diseases.^[14,29,30] Their applications have not yet been documented in cardiovascular diseases. In this work, we sought to evaluate the efficiency of the disk-shaped, relative to the spherical, nanoparticles in marginating to the vascular endothelia in atheroprone disturbed flow areas by using *in vitro* and *in vivo* modeling systems and identify the therapeutic benefits of shape-optimized and drug-loaded particles in preventing atherosclerosis.

2. Results

2.1. Characterization of Mesoporous Silica Nanosphere and Mesoporous Silica Nanodisk

To elucidate the shape effect on the margination of nanoparticles in disturbed versus laminar flow conditions, Rhodamine

B isothiocyanate (RITC)-labeled highly monodispersed mesoporous silica nanosphere (MSNS) and mesoporous silica nanodisk (MSND) with identical compositions and surface charges but with different shapes were fabricated. The morphology of the particles was characterized using transmission electron microscopy (TEM) (Figure S1A, Supporting Information) and scanning electron microscopy (SEM) (Figure 1A), in which MSNS had a diameter of ≈ 150 nm, and MSND was 180 nm in diameter and 60 nm in thickness (Figure S1B, Supporting Information). The hydrodynamic diameters of MSNS and MSND were both ≈ 150 nm (Figure S1C and Table S1, Supporting Information). The average zeta potential of both particles was ≈ -17 mV (Figure S1D and Table S1, Supporting Information). These data indicated that MSNS and MSND are similar in physical properties except for the shape. Dose-response tests showed that MSNS and MSND at 10–200 $\mu\text{g mL}^{-1}$ did not affect the cell viability and that there was no significant difference between MSNS and MSND (Figure S1E, Supporting Information). Deposition of the MSNS/MSND nanoparticles to human umbilical vein endothelial cells (HUVECs) surfaces in a static condition was visualized by laser confocal imaging. Measuring the fluorescent intensity of the particle-incubated cells, without washing with buffer, indicated no statistical difference in the deposition of MSND and MSNS to the cells after 1 h of incubation (Figure S2A, Supporting Information). However, greater binding of MSND than MSNS to the cells was indicated by incubation of the cells at 4 °C to inhibit the active cellular uptake followed by washing out the unbound particles (Figure S2B, Supporting Information). At 37 °C, confocal imaging in the treated cells with several washes demonstrated a more pronounced uptake of MSND than MSNS (Figure S2C, Supporting Information). Cellular uptake of nanoparticles was also quantitatively determined by flow cytometry, and the cells with a strongly positive RITC signal were counted and expressed as a percentage of the total number of cells (Figure S2D, Supporting Information). In agreement with the confocal imaging data, MSND entered the cell more profusely than MSNS (Figure 1B). To directly visualize intracellular trafficking of the nanoparticles, cells were incubated with MSNS or MSND for 1 h, followed by several washes and then immunofluorescence to determine their intracellular locations in relation to various subcellular compartments including endosomes (indicated by endosome markers EEA1, RAB5A or RAB7A) and lysosomes (indicated by the LysoTracker) (Figure 1C,D and Figure S3, Supporting Information). Confocal imaging of the treated cells and the quantification revealed stronger colocalization of the fluorescent signals from the early endosomes (EEA1/RAB5A) and MSND and that the proportion of MSND-colocalized endosomes ($\approx 62\%$) was significantly higher than that of MSNS ($\approx 19\%$) (Figure 1C and Figure S3A, Supporting Information), suggesting more profound accumulation of MSND than MSNS in the early endosomes. Similarly, the proportion of MSND-colocalized lysosomes ($\approx 34\%$) was greater than that of MSNS ($\approx 15\%$) (Figure 1D). Calculating the colocalization of MSND and MSNS with the early endosomes, late endosomes, and lysosomes (the proportion of RAB5A-, RAB7A- or LysoTracker-colocalized nanoparticles) suggested a promoted endosomal/lysosomal escape of MSND over MSNS (Figure S3C,

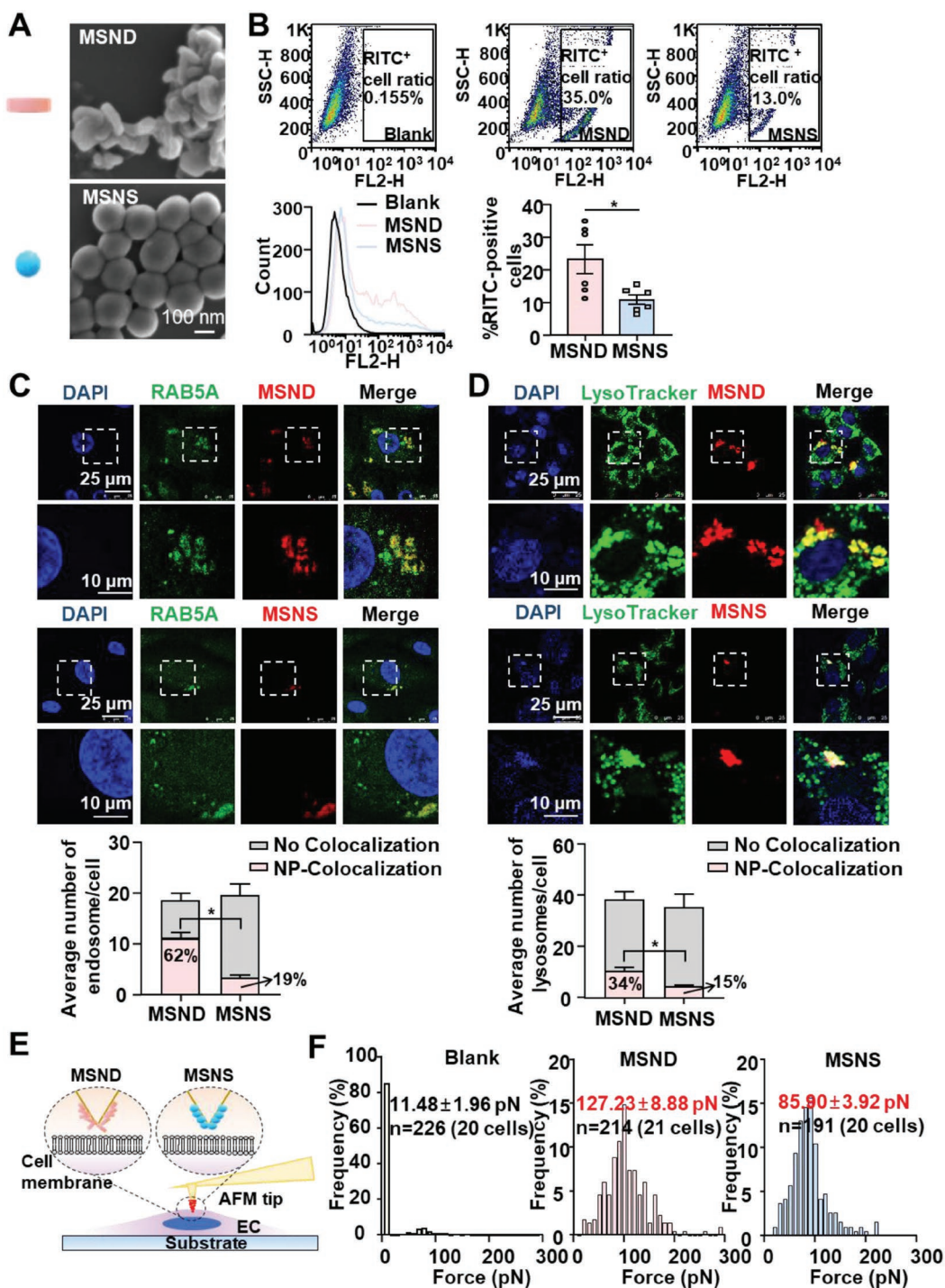


Figure 1. The mesoporous silica nanodisk (MSND) and mesoporous silica nanosphere (MSNS) adhesion to and uptake by endothelial cells in a static condition. A) Representative SEM image of MSND and MSNS. The yellow arrow indicates the view on the thickness side, and the white arrow indicates the view on the circular side. B) Flow cytometry evaluation of the absorption efficiency of MSND and MSNS by HUVECs. Cells were incubated with PBS (as a blank), MSND, or MSNS for 1 h. In the representative dot-plot diagrams obtained by flow-cytometric analysis, the x- and y-axis show the fluorescence intensities of RITC and cell number, respectively. Cells with a positive RITC signal were counted and expressed as a percentage of the total number of cells. $n = 6$. C, D) Representative confocal images showing colocalization of MSND/MSNS with early endosomes (as indicated by RAB5A) and lysosomes (as shown by LysoTracker). Nuclei were stained with DAPI and nanoparticles appeared red. Colocalization is shown in yellow. Bar charts in the lower panels are statistics of the proportion of nanoparticle-colocalized endosomes/lysosome and the proportion of non-colocalized endosome/lysosomes. In (C), $n = 16$ and 15; in (D), $n = 20$ and 15. E) Schematic representation of a cell adhered to a substrate and a modified AFM probe coming in contact with the cell membrane in a liquid environment. MSNS/MSND nanoparticles were modified onto the AFM probe. F) The force values obtained from ≈ 200 force–distance curves were compiled in force distribution histograms. The most probable force of interaction was defined by the maximum of the Gaussian fit to each histogram. $n = 226$, 214, and 191. Data are presented as mean \pm SEM. * $p < 0.05$ by Student's t -test.

Supporting Information). In summary, no difference between MSNS and MSND in deposition was found in a static condition; MSNS and MSND both adopt the conventional endolysosomal route of trafficking, while MSND exhibits a more efficient endothelial uptake than MSNS.

2.2. Quantification of the Force of Nanoparticle–Cell Membrane Interactions

Nanoparticle internalization begins with an initial adhesion to the cell membrane.^[31] Weak adhesion interaction may lead to preserved cellular uptake efficiency and/or failed cellular uptake upon mechanical force exposure.^[32] To characterize the adhesion of the nanoparticle toward the cell membrane and to determine whether this is modulated by the particle shape, we quantitated the adhesion force between MSNS/MSND and the cell membrane by atomic force microscopy (AFM). The schematics of the force detection process are shown in Figure 1E. MSNS and MSND were separately modified onto the AFM probes by a method described by Demokritou et al.^[33] The morphology of the nanoparticle-coated AFM probes was revealed by SEM (Figure S4A, Supporting Information). Forces between the non-coated (blank) or nanoparticle-coated tips and the cells were acquired at the nucleus and successive force–distance curves were obtained following a standard approach–retraction operation (Figure S4B, Supporting Information). Quantification of the force of interaction demonstrated significant differences in the relative adhesion force of the none control, MSND, and MSNS with cell surfaces. The adhesion force measured with non-coated tips was 152 (maximum) and 0 pN (minimum); the force of MSND was 969 (maximum) and 13 pN (minimum), and MSNS was 632 (maximum) and 13 pN (minimum). Furthermore, the force values obtained from ≈ 200 force curves were subjected to force distribution histogram presentation. The most probable force of interaction was defined by the maximum of the Gaussian fit to each histogram. The ensemble-averaged adhesive forces for blank, MSNS, and MSND were 11.48 ± 1.96 , 85.90 ± 3.92 , and 127.23 ± 8.88 pN, respectively (Figure 1F). Compared to the sphere-shaped MSNS, the disk-shaped MSND displayed a much stronger adhesive interaction with the cell membrane, which may explain their higher cellular uptake efficiency.

2.3. The Effect of Particle Shape on their Margination Propensity under Hemodynamic Conditions

To determine whether MSNS/MSND nanoparticles can target the disturbed flow areas and whether the particle shape affects their margination under hemodynamic conditions, we performed in vitro studies by utilizing two modeling systems (Figure 2A,B). First, a vertical-step flow chamber, as described by Chiu et al.^[34] was employed to produce disturbed or laminar flow in different regions of one chamber. In this model, flow separation occurs in the region proximal to the step, mainly forming the disturbed flow area that ranges from the step to the reattachment point-adjacent region and the laminar flow area that starts from the reattachment point-adjacent region to

the very distal region (Figure 2A). A 3D microfluidic vascular stenosis model, as reported by Ingber et al.,^[21] was also used to produce disturbed or laminar flow by mimicking regions of living blood vessels with 90% lumen obstruction (Figure 2B). In this model, geometric obstruction generates a ≈ 100 -fold increase in shear stress at the stenotic site. The stenotic area with a high and unidirectional shear stress is considered to be a laminar flow area, whereas the just downstream of the narrowed region with low and reciprocating shear stress is a disturbed flow area. PBS buffer or culture medium containing MSNS or MSND at a concentration of $20 \mu\text{g mL}^{-1}$ was perfused through the vertical-step flow device at a constant flow rate of $500 \mu\text{L s}^{-1}$ for 1 h. Laser confocal imaging indicated that both particles preferentially accumulated in the disturbed flow area, no matter whether endothelial cells were present or not (Figure 2C,D). Intriguingly, MSND showed a higher trend in the margination compared to MSNS (Figure 2C,D). To determine the difference statistically, we calculated the mean fluorescence intensity (MFI) of nanoparticles in the disturbed versus laminar flow areas and demonstrated a significantly higher adhesion density of MSND than that of the MSNS (Figure 2E). Co-staining of the nucleus or the endothelial marker VE-cadherin indicated similar cell density in both areas (Figure 2D,E). In the microfluidic model of vascular stenosis, we observed in real-time that perfusion of MSNS or MSND at a concentration of $20 \mu\text{g mL}^{-1}$ in PBS buffer or culture medium through the device at a flow rate of $10 \mu\text{L min}^{-1}$ resulted in a gradual accumulation of both particles downstream of the stenotic site, where disturbed flow develops; notably, the difference between MSNS and MSND became progressively more evident as time goes on (Figure 2F,G). The results from both models suggest that the margination propensity of the disk-shaped MSND nanoparticles is significantly higher than that of the sphere-shaped MSNS in the disturbed flow areas.

2.4. The Effect of Particle Shape on their Targeted Delivery to the Disturbed Flow Regions In Vivo

To evaluate the targeted delivery capacity of nanoparticles to the atheroprone vascular endothelia in vivo, we utilized a carotid partial ligation mouse model, which has been generally used to create disturbed blood flow in the common carotid arteries where flow disturbance does not naturally appear (Figure 3A). Wildtype mice on a C57BL/6 background were surgically operated on the first day. On the second day, each mouse was injected with MSNS or MSND via the right jugular vein immediately after its left carotid artery was exposed to a somatic fluorescence microscope (Figure 3B). Real-time fluorescence angiography visualized rapid and sustained adherence of MSND to the vascular walls of the ligated arteries (Figure 3C and Video S1, Supporting Information). Although MSNS also adhered to the vessel walls, the fluorescence-positive area and fluorescence intensity of MSNS were much less than that of MSND (Figure 3C,D and Video S2, Supporting Information). In unligated mice, both particles passed rapidly through the common carotid arteries with little adhesion (Videos S3 and S4, Supporting Information). These observations demonstrate specific targeting of the disk-shaped, but not the sphere-shaped

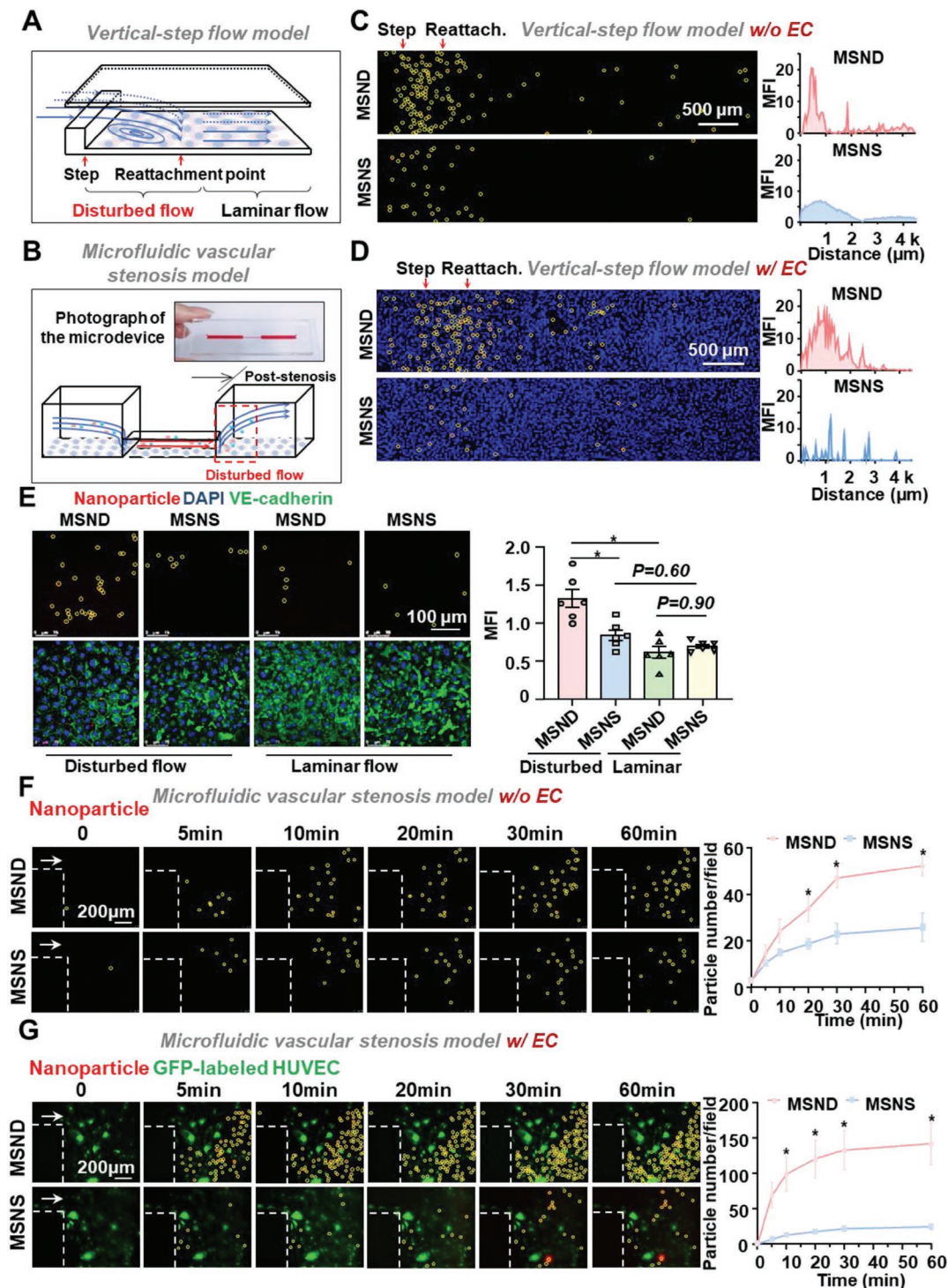


Figure 2. The margination behavior of nanoparticles under hemodynamic conditions. A) Schematic diagram of the vertical-step flow chamber. The step and the reattachment point are indicated by red arrows. The disturbed flow and laminar flow areas are also illustrated. B) Schematic diagram of the microfluidic vascular stenosis model (lower panel) and photograph of the microdevice fabricated with PDMS (upper panel). The disturbed flow area in one microdevice is illustrated. C, D) Confocal images showing particle deposition in the vertical-step flow chamber without HUVEC (C) or with HUVEC seeding (D). Nuclei were stained with DAPI, nanoparticles were labeled with RITC, and yellow circles were used to highlight the adherent nanoparticles. Quantification of the mean fluorescence intensity (MFI) of nanoparticles is shown in the right panels. In (C), $n = 4$, and in (D), $n = 4$. E) Representative images with high magnification showing particle deposition in the disturbed versus laminar flow area. Quantification of the MFI is shown in the right panel. Yellow circles were used to highlight the adherent nanoparticles. $n = 6$. F, G) Confocal images showing the particle deposition in the microfluidic vascular stenosis model without HUVEC (F) or with HUVEC seeding (G). Quantification of the particle number for the indicated duration of time is shown in the right panel. Statistical significance was tested between MSND and MSNS. Yellow circles were used to highlight the adherent nanoparticles. In (F) and (G), $n = 5$. Data are presented as mean \pm SEM. $*p < 0.05$ by two-way or one-way ANOVA followed by Tukey's post-hoc test.

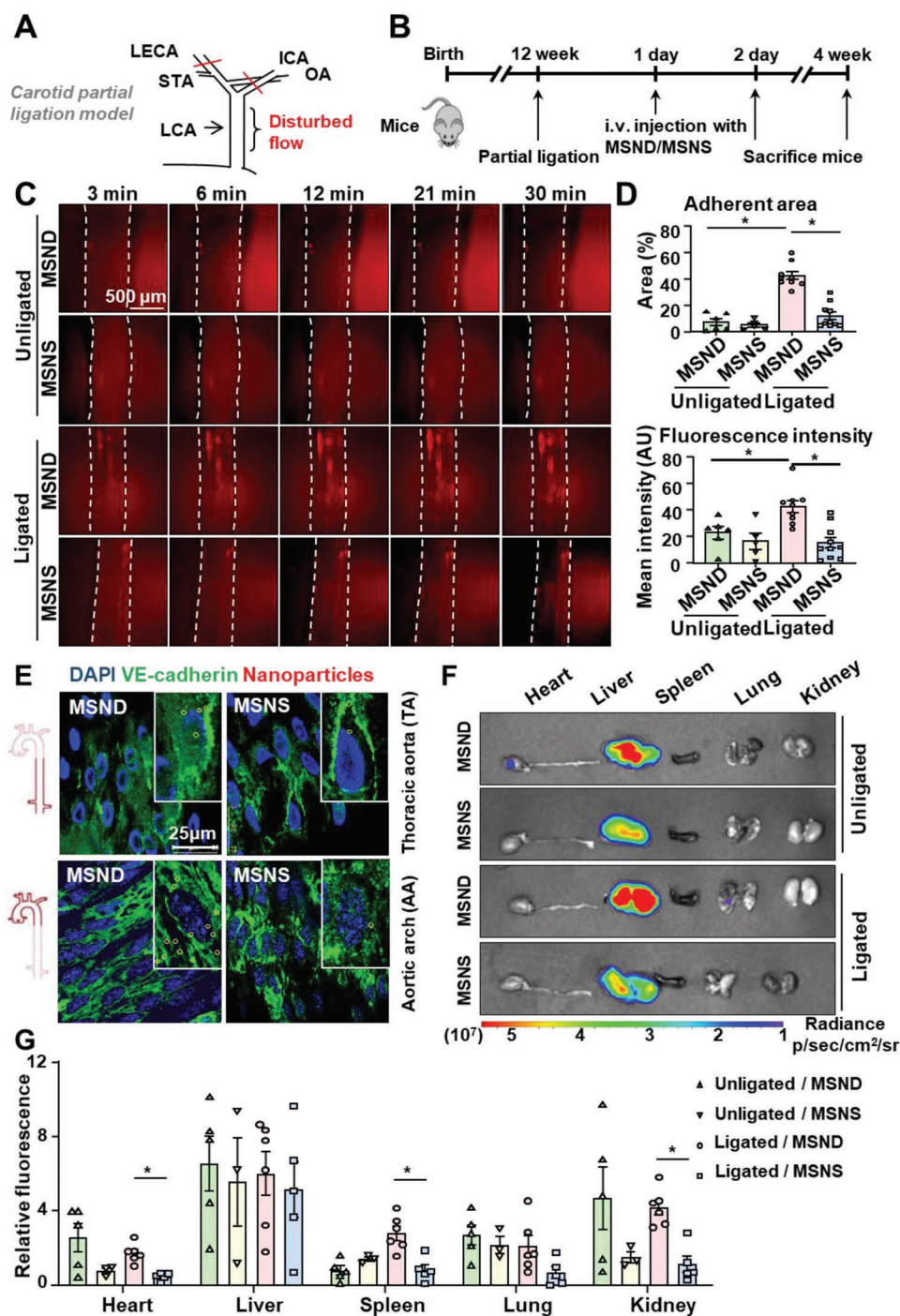


Figure 3. In vivo assessment for targeted delivery of nanoparticles in mice. A) Schematic diagram of partial carotid ligation in the mouse. LCA: left carotid artery; OA: occipital artery; ICA: internal carotid artery; LECA: left external carotid artery; STA: superior thyroid artery. B) Schematic diagram of experimental timeline. Mice were subjected to MSND/MSNS administration 1 day after the ligation surgery and then real-time fluorescein angiography visualization. The mice were sacrificed immediately or 4 weeks after fluorescein angiography for different purposes. C) Representative fluorescein angiography images showing MSND/MSNS (labeled with RITC) adhesion to or flowing through the common carotid arteries. Images were captured within 30 min from the starting point. $n = 6, 5, 9, 10$, respectively. Dash lines indicate the vessel walls. D) Quantification and statistics of adherent area and mean fluorescence intensity of MSND/MSNS in (C). E) Representative confocal images showing en face immunofluorescence of endothelial marker VE-cadherin, MSND/MSNS, and the nuclei (DAPI). Yellow circles were used to highlight the adherent nanoparticles. F) Assessment of in vivo biological distribution of MSND and MSNS in mice. The mice were subjected to carotid partial ligation or sham surgery. $n = 5, 3, 6$, respectively. G) Quantification of the mean fluorescence intensity in the major organs in (F). Data are presented as mean \pm SEM. $*p < 0.05$ by two-way ANOVA followed by Tukey's post-hoc test.

nanoparticles, to the arterial regions with disturbed blood flow. The findings were further validated in the mouse descending thoracic aorta and aortic arch, regions of naturally developed laminar versus disturbed flow areas.^[35] In the descending thoracic aorta, both MSNS and MSND barely deposited; in contrast, evident deposition of MSND was found in the inner curvature of the aortic arch (Figure 3E). One day after the above operation, nanoparticle biodistribution was assessed in various organs, including the heart and aorta, liver, spleen, lung, and kidney, by analyzing the emitted radiation. Higher accumulation was observed in the heart and aorta, spleen, and kidney with the disk-shaped MSND (Figure 3F,G). We also evaluated the long-term biological effect of the administration of MSNS/MSND. Hematoxylin and eosin (H&E) staining revealed no obvious organ toxicity in the heart, liver, spleen, lung, or kidney at 1-month post-injection of the particles (Figure S5, Supporting Information). These results provide experimental evidence showing that the disk-shaped nanoparticle can be used to target atheroprone endothelia in vivo, in addition to providing a method to locate and image these endothelia in situ.

2.5. Assessment of DAC-Loaded MSND and MSNS Nanoparticles (MSND-DAC and MSNS-DAC) in Inhibiting Endothelial Inflammation

To evaluate the functional potential of MSNS/MSND, we loaded nanoparticles with DAC, an epi-immunotherapeutic agent that has anti-inflammatory activity^[36] (Figure 4A). The absorbance of DAC in the supernatant was measured by using UV-vis spectrophotometer at 240 nm and both particles exhibited an excellent drug loading efficiency ($\approx 10\%$) (Table S1, Supporting Information), probably due to their hollow structure. Moreover, MSND-DAC and MSNS-DAC displayed similar release profiles, indicating $\approx 65\%$ of DAC was released within 72 h in incubation with PBS buffer (pH 7.4) (Figure 4B). We performed the MTT test to assess the cytotoxicity of MSND-DAC or MSNS-DAC at concentrations of 10–200 $\mu\text{g mL}^{-1}$ and found that DAC loading did not induce cytotoxicity, compared with the empty MSNS or MSND (Figure 4C). To explore the anti-inflammation effects of MSND-DAC and MSNS-DAC under hemodynamic environments, a culture medium containing MSNS/MSND or MSND-DAC/MSNS-DAC at a concentration of 20 $\mu\text{g mL}^{-1}$ was perfused through the vertical-step flow device at a constant flow rate of 500 $\mu\text{L s}^{-1}$ for 6 h. Immunofluorescence staining followed by confocal imaging indicated that the expression of pro-inflammatory adhesion molecules ICAM1 and SELE was profound in the disturbed flow area, while their expression could be suppressed by MSND-DAC/MSNS-DAC; MSND-DAC exhibited a much greater inhibitory effect than MSNS-DAC (Figure 4D and Figure S6, Supporting Information). As DAC functions primarily via inhibiting the DNA methyltransferases (DNMTs),^[37] we detected the expression of DNMT family proteins DNMT1, DNMT3A, and DNMT3B in the DAC-, nanoparticle-, or DAC-loaded nanoparticle-treated HUVECs. The results showed that either DAC or MSND-DAC/MSNS-DAC could inhibit the expression of DNMT1 and DNMT3A, but not DNMT3B (Figure 4E). These findings demonstrate an anti-inflammation potential of

the DAC-loaded nanoparticles, in particular MSND-DAC, in treating the atheroprone endothelia.

2.6. In Vivo Assessment of the Anti-Atherosclerotic Efficacy of the MSND-DAC/MSNS-DAC Nanoparticles in Hypolipidemia Mice

To test the ability of this shape-optimized nano-delivery system to function as an anti-atherosclerotic agent, ApoE^{-/-} mice were subjected to carotid partial ligation to induce disturbed blood flow in the common carotid arteries and fed on a high-cholesterol diet to build up a disturbed flow-accelerated atherosclerosis model, followed by PBS, DAC (0.2 mg kg⁻¹), MSNS, MSNS-DAC, MSND, MSND-DAC (2 mg kg⁻¹) injection via the caudal vein twice a week for 4 weeks (Figure 5A). This dose of MSND/MSNS-DAC in mice (2 mg kg⁻¹) is comparable with the dose of DAC (0.2 mg kg⁻¹) according to average drug loading efficiency (Table S1, Supporting Information). The atherosclerotic areas in the aortic tree were reduced by DAC, MSNS-DAC, and MSND-DAC, and the reduction was especially profound in the left common carotid artery, where disturbed blood flow is induced by carotid partial ligation (Figure 5B). Moreover, histological examination of cross-sections of left common carotid arteries indicated that plaque formation (evidenced by the intima-to-media ratio), lipid accumulation (revealed by Oil red O staining), and monocyte/macrophage infiltration to the vessel wall (represented by the CD68-positive area to the plaque area) were markedly alleviated by DAC, MSNS-DAC, or MSND-DAC (Figure 5C–E). Notably, the intima-to-media ratio and monocyte/macrophage infiltration in the DAC-treated mice were reduced by 55.4% and 37.2%, respectively; they were reduced by 78.3% and 64.4% in the MSND-DAC-treated mice, while reduced by 55.2% and 39.8% in the MSNS-DAC-treated mice (Figure 5D,E). These data suggest that the disk-shaped MSND loaded with DAC can facilitate the beneficial effect of DAC in treating atherosclerosis.

2.7. In Vivo Toxicity Assessment of the DAC-Loaded Nanoparticles in ApoE^{-/-} Mice

A major advantage of nanoparticle-mediated drug delivery systems is their ability to enhance the biosafety of the systemically administrated therapeutic agents.^[38] As a chemotherapeutic drug, DAC has been reported to have strong toxicity and side effects in the bone marrow hematopoietic system and nervous system for a long-time systemic application.^[27] We prepared tissue sections of the heart, liver, spleen, lung, and kidney obtained from ApoE^{-/-} mice subjected to the PBS, DAC, MSNS, MSNS-DAC, MSND, and MSND-DAC treatments and the H&E staining of them did not reveal noticeable lesion or abnormality (Figure 6A). We further found that the red blood cell number was significantly decreased in the DAC-treated mice, in line with the previous report,^[39] and that the hematopoietic toxicity of DAC could be eliminated by nanoparticle-enclosing (Figure 6B). A complete blood routine report is also shown (Table S2,

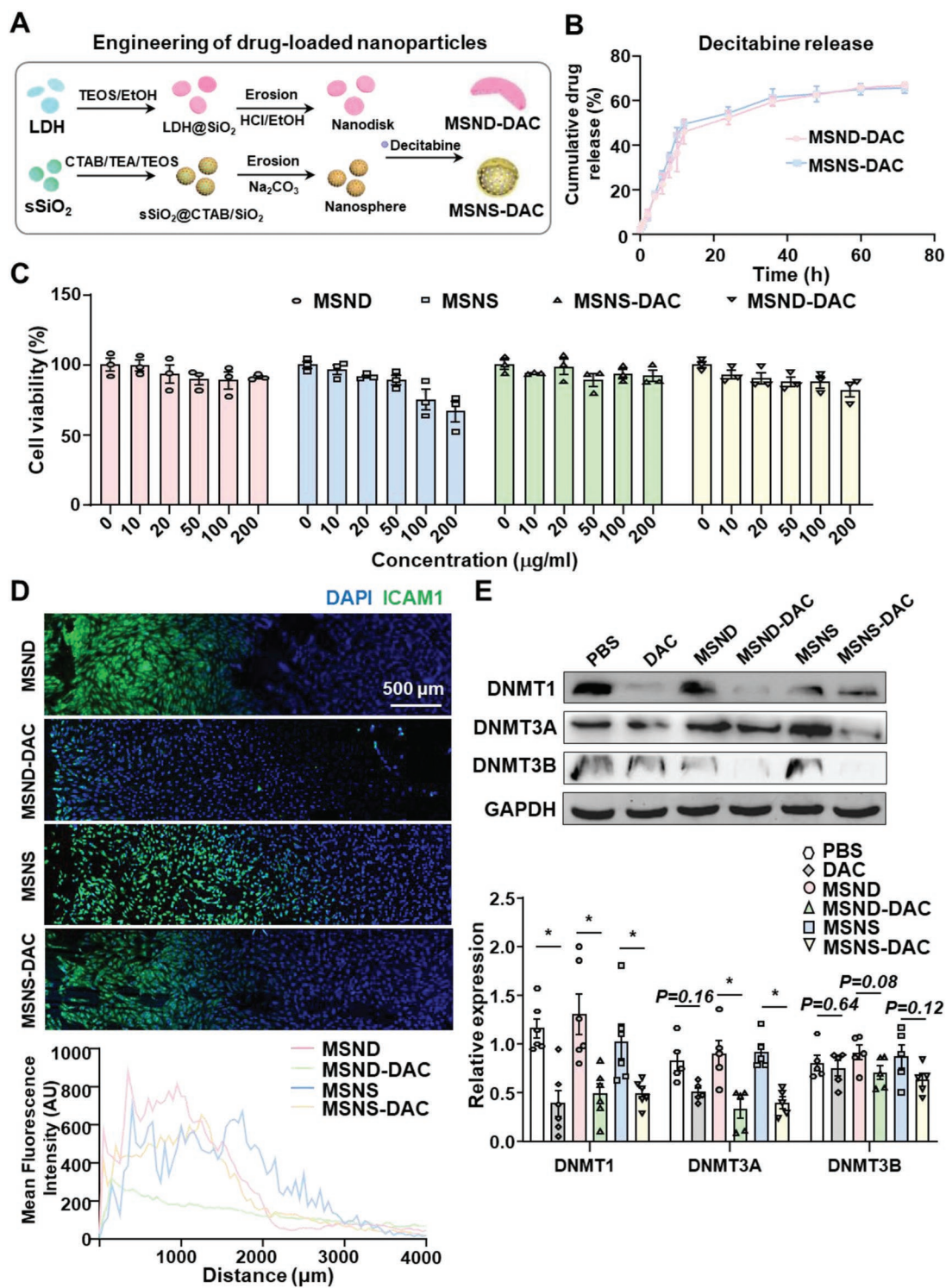


Figure 4. In vitro assessment of the anti-inflammation efficacy of the decitabine-loaded nanoparticles. A) Schematic diagram showing engineering of 5-Aza-2'-deoxycytidine (Decitabine, DAC)-loaded MSND/MSNS. B) DAC release profile probed at different time points. $n = 3$. C) Assessment of the viability of HUVECs treated with MSND, MSNS, MSND-DAC, and MSNS-DAC at concentrations of 10–200 $\mu\text{g mL}^{-1}$ for 24 h. The cell viability percentage of the treated cells was calculated relative to that of the untreated cells (with arbitrarily assigned 100% viability). $n = 3$. D) Confocal images showing the immunofluorescence of the pro-inflammatory gene ICAM1 and the nuclei (DAPI) in the vertical-step flow device. Cells were subjected to perfusion of media with MSND-DAC and MSNS-DAC (20 $\mu\text{g mL}^{-1}$) for 6 h. The mean fluorescence intensity of ICAM1 is calculated and shown in the lower panel. E) Western blotting showing the expression of DNMT1, DNMT3A, and DNMT3B in HUVECs incubated with PBS, DAC (2 $\mu\text{g mL}^{-1}$), MSNS, MSNS-DAC, MSND, and MSND-DAC (20 $\mu\text{g mL}^{-1}$) for 24 h. Semi-quantification of the blots is shown in the lower panel. $n = 6$ or 5. Data are presented as mean \pm SEM. $*p < 0.05$ by two-way ANOVA followed by Tukey's post-hoc test.

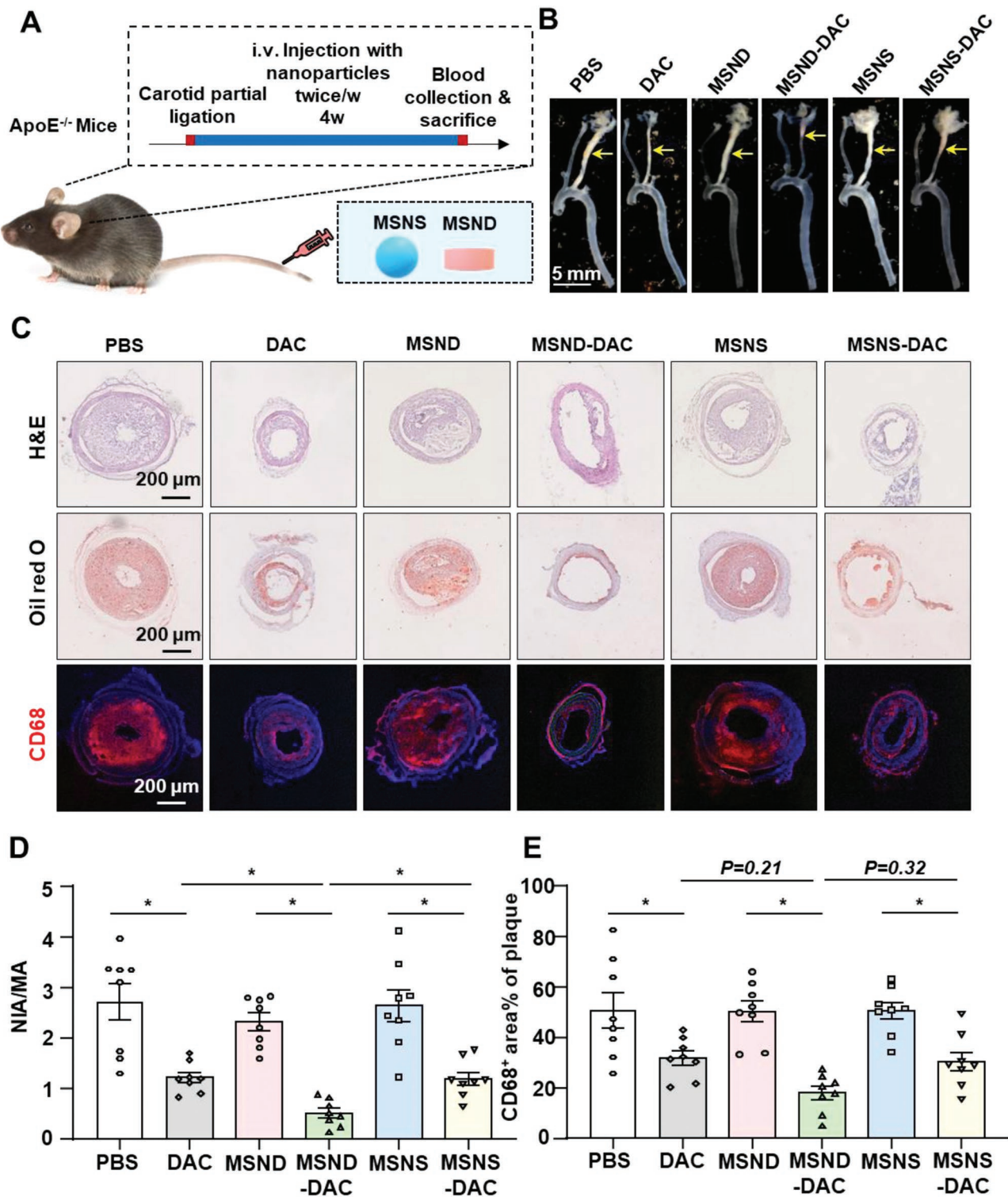


Figure 5. In vivo assessment of the anti-atherosclerotic efficacy of the decitabine-loaded nanoparticles in ApoE^{-/-} mice. A) Schematic diagram of disturbed flow-accelerated atherosclerosis model. B) Representative gross images of the aorta, brachiocephalic artery, and carotid artery from ApoE^{-/-} mice treated with PBS, decitabine (DAC, 0.2 mg kg⁻¹), MSNS, MSNS-DAC, MSND, or MSND-DAC (2 mg kg⁻¹). Mice were subjected to intravenous injection from the caudal vein with the above agents twice a week for 4 weeks. $n = 8$. C) Cross-sections of the carotid artery were stained with hematoxylin and eosin (H&E) and Oil red O to analyze plaque formation and lipid accumulation, respectively. Immunofluorescence of CD68 indicates monocyte/macrophage infiltration. D,E) Quantification and statistic of the intima-to-media ratio and the percentage of CD68-positive areas in (C). Each dot represents the average value obtained from at least three different parts of one carotid artery. $n = 8$. Data are presented as mean \pm SEM. * $p < 0.05$ by Brown–Forsythe and Welch ANOVA test or one-way ANOVA followed by Tukey’s post-hoc test.

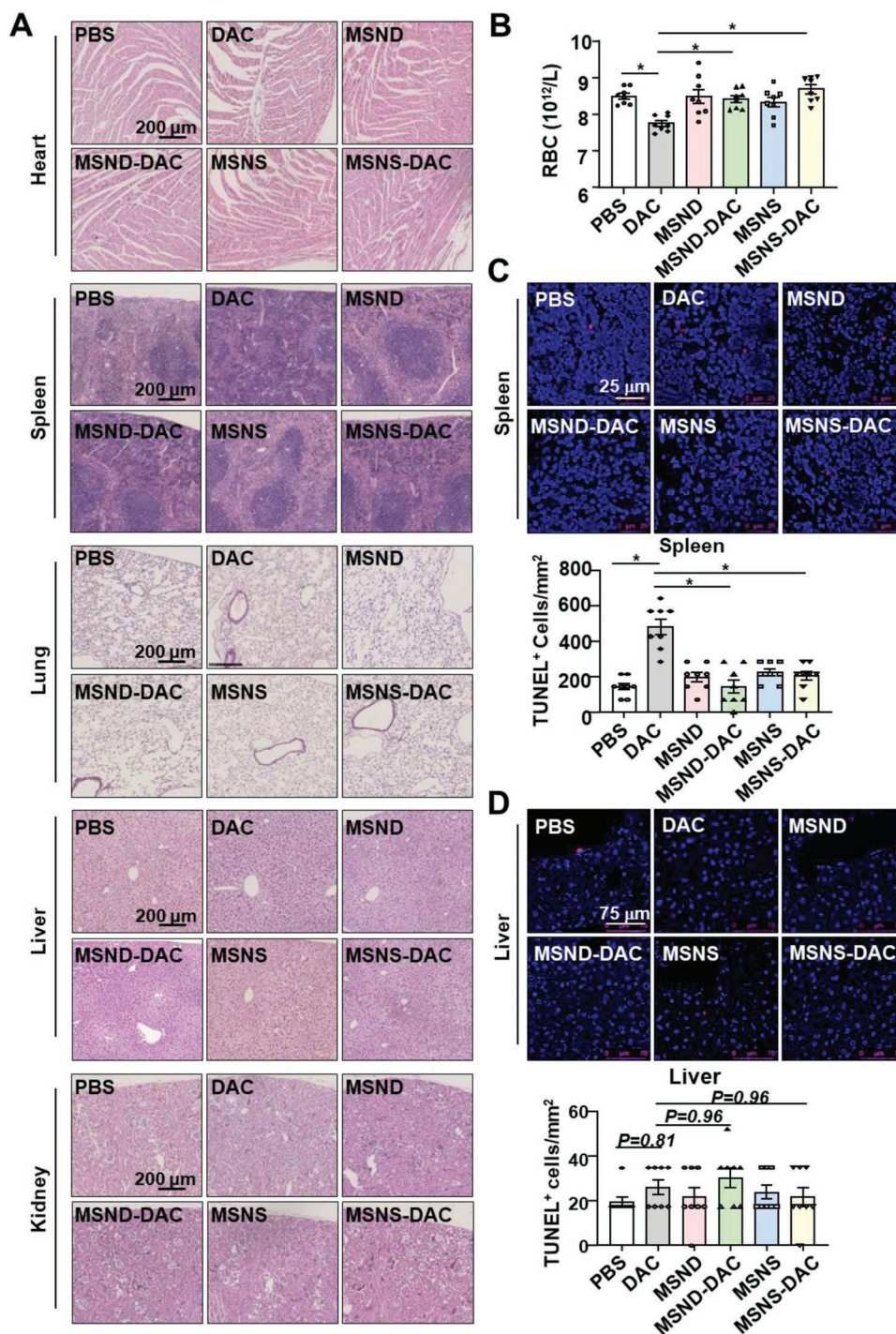


Figure 6. In vivo toxicity assessment of decitabine-loaded nanoparticles in ApoE^{-/-} mice. A) H&E staining of the major organs from ApoE^{-/-} mice treated with PBS, decitabine (DAC, 0.2 mg kg⁻¹), MSNS, MSNS-DAC, MSND, MSND-DAC (2 mg kg⁻¹) for 4 weeks. *n* = 8. B) The average circulating red blood cell (RBC) count in ApoE^{-/-} mice treated with the drug-loaded nanoparticles. *n* = 8. C) TUNEL staining in spleen from mice with the indicated treatments. Quantification of the number of TUNEL-positive cells per unit area is shown in the right panel. *n* = 8. D) TUNEL staining in the liver from mice with the indicated treatments. Quantification of the number of TUNEL-positive cells per unit area is shown in the right panel. *n* = 8. Data are presented as mean ± SEM. **p* < 0.05 by one-way ANOVA followed by Tukey's post-hoc test.

Supporting Information). To ascertain whether the decrease in red blood cells is due to dysfunction or damage of the hematopoietic organs before any visible lesion formation, we performed TUNEL staining in the sections from the spleen

and liver to assess apoptosis. In the spleen, TUNEL-positive apoptotic cells reached 463 per square millimeter area in the specimens from the DAC-treated mice, while decreased to 157 or 199 from the MSND-DAC- or MSNS-DAC-treated

mice, respectively, indicating that nanoparticle-enclosing could effectively reduce the drug toxicity (Figure 6C). In the liver, no significant difference in TUNEL-positive cell number was detected (Figure 6D).

3. Discussion

Blood flowing through the arteries with narrowed geometries or high curvatures and branching causes the formation of disturbed flow patterns, that is, flow reduction, oscillation, and disturbance, leading to vascular endothelial activation and chronic inflammation. Disk-shaped circulating platelets preferentially aggregate and deposit at the adjacent endothelial surface downstream of vessel obstruction where disturbed blood flow occurs.^[40] Taking this inspiration, we constructed the disk-shaped mesoporous silica nanoparticles MSND, attempting to improve their specific delivery efficacy to the disturbed flow-activated endothelia. The sphere-shaped MSNS nanoparticles were compared. Analyzing nanoparticle adhesion to and uptake by endothelial cells under a static condition indicated that, first, particle shape did not influence the deposition behavior of MSNS/MSND in static, as suggested by confocal imaging of the particle-incubated cells (w/o wash with buffers). Second, MSND could be taken up by HUVECs and undergo endolysosomal intracellular trafficking in a more efficient way, as evidenced by immunofluorescent staining of endosome and lysosome markers and visualization of the particles. We, therefore, speculated that disk shape might facilitate MSND adhesion to the cell membrane and that a strong adhesion force between the particle and cell membrane could help maintain their interaction. To test this, we performed an AFM experiment to quantitate the adhesion force between MSNS/MSND and cell membrane and demonstrated stronger forces for MSND than MSNS, probably due to higher surface binding of the non-spherical particle.^[41] The findings are in line with previous reports exploring a shape-effect on nanoparticle-cell membrane interaction by using the AFM technique,^[42] providing an explanation for the higher cellular uptake efficiency of MSND than MSNS.

Notably, deeper insights were gained from utilizing two *in vitro* models that are able to simulate complex hemodynamic conditions, in particular the disturbed flow patterns, to sufficiently address the effects of particle shape on the margination propensity of nanoparticles. The vertical-step flow device and microfluidic device represent comprehensive strategies to reproduce shear stress as those found in arterial stenosis, curvatures, and branching. In the vertical-step flow device (in the presence or absence of cells), both MSNS and MSND preferentially accumulated in the disturbed flow area, and this effect was much more profound for MSND, proving the influence of shear stress on the margination performance of nanoparticles and the dependence of this influence on the particle shape. This influence might not be attributable to the activation of endothelial cells by disturbed flow, although such a mechanism has been reported by others, for example, Wang G et al. have indicated that disturbed flow induces particle adhesion to and uptake by endothelial cells via activating cell endocytosis.^[43] Our data obtained from the cell-coated and free-cell vertical-step flow devices suggest that endothelial activation by disturbed flow is not the primary

cause of the diversity of margination propensity of nanoparticles. Instead, the flow field itself is an important factor to take into account, related to particle deposition and adhesion. Greater shear stress as presented in the laminar flow area may cause lower adhesion of the nanoparticle to the cell membrane due to the decoupling forces derived from the hydrodynamic forces.^[44,45] Moreover, shaping nanoparticles into non-spherical (rod, disk, needle, ellipsoid, hemisphere) has been reported to induce significant margination in the presence or absence of external forces.^[14,17,46–48] In addition, by using the microfluidic device, we were able to evaluate the shape effects on particle margination in physiological and pathophysiological more-relevant conditions in a real-time manner. Similar phenomena have been observed, compared with the vertical-step flow device. Our findings suggest that the disk shape offers a clear advantage over the sphere shape in terms of targeting the disturbed flow area.

It is also noticeable that we tested the translation of the *in vitro* shape effects to *in vivo* conditions. Indeed, the behavioral changes of nanoparticles under complicated hemodynamic flow *in vivo* were rarely studied previously due to the lack of appropriate animal models. Here, we innovatively used a surgically induced disturbed blood flow model in a mouse to investigate the potential shape-effect of disk and sphere. RITC-labeled MSND and MSNS were injected through the right jugular vein and real-time fluorescence imaging of the ligated or unligated carotid arteries allowed capturing the dynamic accumulating events of MSND and MSNS at the disturbed versus laminar flow regions. Besides, the detection of MSND and MSNS at the natural curvatures and straight parts of the mouse aorta was carried out. Results from both studies indicated that shape is a crucial parameter that may determine the margination behavior of nanoparticles *in vivo*. Specifically, the disk-shaped MSND preferentially accumulated in the partially ligated left common carotid artery and the inner curvature of the aortic arch, where a disturbed flow pattern is prominent. Further assessing the nanoparticle biodistribution in various organs indicated a high accumulation in the liver but no significant difference between shapes, which might be attributable to those small vessels in the liver might capture the nanoparticles for further processing without distinguishing their shapes.^[48] Indeed, most nanoparticles usually accumulate in the liver.^[49] Heart, lung, and kidney exhibited significant differences between shapes. Overall, the accumulation of disk-shaped MSND in the main organs was greater than that of MSNS, in agreement with our *in vitro* findings.

Unacceptable adverse side effects have hindered the application of the hypomethylating agent DAC in treating cardiovascular diseases including atherosclerosis.^[26] Finally and most importantly, in this study, we have proved that DAC encapsulated within mesoporous silica nanoparticles can alleviate its cytotoxicity and that shaping the particle to disk can facilitate targeted delivery of DAC to the atheroprone endothelia. In a hyperlipidemia mouse model accompanied by carotid partial ligation to induce disturbed flow, DAC-loaded nanoparticles decreased apoptosis in the spleen and reversed the reduction in red blood cell number, compared with the “naked” DAC. Although no apparent damage to the main organs was observed, as indicated by the immunohistochemical staining, the cellular functional abnormality may appear before the development of any morphological changes. Furthermore,

MSND-DAC treated mice had significantly decreased thickening of the common carotid arteries, limited lipid accumulation in the plaque, and reduced monocyte/macrophage infiltration to the vessel walls, compared with the empty nanoparticle, the “naked” DAC, or the sphere-shaped MSNS-DAC. These effects might be explained by the anti-inflammation activity of DAC in endothelial cells via depleting an atherogenic protein DNMT1 that has been previously proved,^[24] and are also consistent with our in vitro studies showing inhibition of endothelial pro-inflammatory molecules by DAC-loaded MSNS/MSND.

In summary, we fabricated disk- and sphere-shaped mesoporous silica nanoparticles (MSND vs MSNS) and designed comprehensive in vitro and in vivo experiments to evaluate the shape effect on targeted delivery of drug-loaded nanoparticles to the disturbed flow regions in vasculature. The results demonstrate preferential accumulation of MSND to the atheroprone vascular endothelia and identify the therapeutic benefits of shape-optimized and drug-loaded nanoparticles in preventing endothelial inflammation. Our study opens new therapeutic opportunities for further studies using this strategy in pre-clinical research and provides useful guidelines for the future rational engineering of drug-loaded nanoparticles in atherosclerosis treatment.

4. Experimental Section

Antibodies and Reagents: Tetraethoxysilane (TEOS) and cetyltrimethylammonium bromide (CTAB) were purchased from Sinopharm Chemical Reagent Co., Ltd. (Shanghai, China). RITC was obtained from Dalian Meilun Biotechnology Co., Ltd. 3-aminopropyltriethoxysilane (APTES) was obtained from Aladdin. DAC was purchased from Selleck (Shanghai, China). Primary antibodies against VE-cadherin (Santa Cruz, sc-9989), SELE (Proteintech, 20894-1-AP), ICAM-1 (Proteintech, 10831-1-AP), RAB5A (Santa Cruz, sc-166600), RAB7A (Beyotime, AF2458), and EEAI (Santa Cruz, sc-137130) were used for immunofluorescence staining. Primary antibodies against DNMT1 (ABclonal, A16729), DNMT3A (ABclonal, A2065), or DNMT3B (ABclonal, A11079) were used for Western blotting.

Synthesis of RITC-Labeled Spherical Nanoparticle Mesoporous Silica Nanosphere: Hollow MSNS were synthesized with solid silica (sSiO₂)-based method.^[50] In brief, sSiO₂ spheres were prepared by adding 6 mL of TEOS into a mixture of 74 mL of ethanol, 10 mL of deionized water, and 3.15 mL of ammonia. After stirring at room temperature for 1 h, sSiO₂ spheres were harvested and dispersed in 10 mL of deionized water by sonication for 15 min. 75 mg of CTAB, 15 mL of deionized water, 15 mL of ethanol, and 0.275 mL of ammonia were added to the sSiO₂ solution, continually stirred for 30 min at room temperature, and then 0.125 mL of TEOS and RITC-APTES were quickly added. After incubation for 6 h at room temperature, the solution was centrifuged at 10 000 rpm for 10 min. The pellets were washed with water and alcohol and resuspended in 10 mL of deionized water to get sSiO₂@CTAB/SiO₂. Finally, Na₂CO₃ was added into the resuspended aqueous solution and vigorously stirred at 50 °C for 10 h to fabricate hollow RITC-MSNS.

Synthesis of RITC-Labeled Disk-Shaped Nanoparticle Mesoporous Silica Nanodisk: Hollow MSND was constructed by a template-based method. First, layered double hydroxide (LDH) nanodisks were synthesized with a nitrates-alkali reaction. A solution of aluminum nitrate and magnesium nitrate hexahydrate was stirred intensely, and a mixed solution of sodium bicarbonate and sodium hydroxide was added drop by drop until the pH value reached 9.5 ± 0.05. Unremittingly stirred for 30 min, the mixture was reacted overnight at 60 °C in an oil bath. After centrifuging and water washing, LDH was resuspended with deionized water. Next, the LDH was coated with CTAB at a ratio of 1:5 (w/w), and 2.5 mL of TEOS and RITC-APTES ethanol solution were added for reaction overnight

to get LDH@SiO₂. Finally, the hollow MSND was harvested after the erosion of LDH@SiO₂ with hydrochloric acid.

Characterization of Nanoparticles: Size and zeta potential were measured by NanoZS (Malvern). The morphology of nanoparticles was directly observed by a Tecnai G2 spirit electron microscope at 120 kV and a field emission SEM (JEOL Ltd., Japan) at 2 kV.

Cell Culture: HUVECs were isolated from the umbilical cords of healthy patients after full-term deliveries. Umbilical cords were obtained with the agreement of the patients and approved by the Peking University People's Hospital Medical Ethics Committee (2015PHB024). HUVECs within passages 5–8 were maintained in Medium 199 supplemented with 10% fetal bovine serum (FBS) (Gemini 900-008), 4 μg mL⁻¹ of endothelial cell growth factor (ECGF) (Sigma E1388), 1% penicillin/streptomycin at 37 °C in an incubator with 95% humidified air, and 5% CO₂ and passaged every 3 days.

MTT Cell Viability Assay: Cells were seeded into 96-well plates at a density of 5 × 10³ cells per well. After being pretreated with PBS, MSNS, or MSND (≈10–200 μg mL⁻¹) for 24 h, MTT (Applygen) reagents were added into the cell culture media to a concentration of 5 mg mL⁻¹. After incubation with the media for 4 h, the supernatant was removed, and 150 μL of DMSO was added to each well. The optical density (OD) at 490 nm was measured.

Quantitative Analysis of Internalized Nanoparticles by Flow Cytometry: To analyze the cellular uptake of MSNS and MSND, cells were cultured in 6-well plates (1 × 10⁵ cells per well) overnight and incubated with MSNS or MSND at a concentration of 100 μg mL⁻¹ for 1 h at 37 °C. In pre-testing the time and concentration (time range of 30 min, 1 h, and 4 h; dose range of 50, 100, and 200 μg mL⁻¹), cells were incubated with the indicated concentration of MSND or MSNS for 1 h or incubated with 100 μg mL⁻¹ MSND or MSNS for the indicated time. The cells were then rinsed with PBS to eliminate the unbound particles. Cells with adherent particles were dissolved with 0.05% trypsin-EDTA solution, washed with PBS three times, and then resuspended in 200 μL of PBS. The percentage of cells with internalized RITC-labeled MSND/MSNS was quantitatively determined by flow cytometer (BD Calibur2, USA).

Immunofluorescent Staining: Cells or tissues were first washed with PBS buffer, fixed in 4% paraformaldehyde (PFA) for 20 min, permeabilized with 0.1% Triton X-100 (in PBS) for 5 min, and rinsed three times. Nonspecific binding was blocked by 3% BSA in PBS for 1 h. Tissues/cells were incubated at 4 °C overnight in an incubation buffer containing 3% BSA and the primary antibodies including VE-cadherin (Santa Cruz, 1:100), CD68 (Abcam, 1:100), SELE (Proteintech, 1:100), ICAM1 (Proteintech, 1:100), RAB5A (Santa Cruz, 1:100), RAB7A (Beyotime, 1:100), or EEAI (Santa Cruz, 1:100). After being washed in PBS three times, the specimens were incubated with Alexa-Fluor 488-conjugated secondary antibody (ThermoFisher, 1:500) for 1 h at room temperature. The fluorescent signals were detected by fluorescence microscopy (Leica DMI6000B; Leica TCS SP8).

Probing Lysosomes and Nanoparticles in Cells: Cells were seeded on a glass bottom dish. 1 mL of serum-free medium containing 20 μg mL⁻¹ of MSND or MSNS, 50 μg mL⁻¹ of LysoTracker Green to allow for labeling of acidic organelles, and DAPI were added into each dish and then incubated at 37 °C for 1 h. The cells were then washed two times with PBS. After that, the cells were examined with a confocal laser microscope (Leica TCS SP8).

Atomic Force Microscopy Measurement of Nanoparticle-Cell Adhesive Forces: AFM probes were modified with MSNS/MSND nanoparticles according to the method developed by Pyrgiotakis et al.^[33] The modified probes were visualized with SEM (JEOL Ltd., Japan). The tips were slowly brought into contact with the nanoparticle suspension for 15–30 touch intervals. Subsequently, the AFM tips were allowed to dry at ambient room conditions and then rinsed with deionized water. For each nanoparticle-cell interaction, three to five sets of tips and cells were used. Five or ten randomly selected cells were investigated during each session. For each cell, 30 to 50 consecutive extension/retraction movements were conducted per cell at a speed of 1000 nm s⁻¹. The forces acting between the cell and the modified tip were measured by bringing the tip into contact at 500 pN. The tip was left in contact (dwell time) for 5 s of each contact.

The Vertical-Step Flow and Adhesion of MSND/MSNS Underflow: This model was adapted from Chiu.^[34] The chamber was composed

of a polycarbonate base plate, two gaskets with different open areas, and a glass slide with a monolayer (bottom), forming a channel with a lesser depth at the entrance, creating a step. The step-flow channel was characterized by a well-defined recirculation Eddy immediately downstream of the step, followed by a region of flow reattachment, and finally, a unidirectional laminar flow that was reestablished further downstream. The chamber containing the cell-seeded glass slide fastened with the gasket was connected to a perfusion loop system, kept in a constant-temperature controlled enclosure, with pH maintained at 7.4 by continuous gassing with a humidified mixture of 5% (vol/vol) CO₂, 20% (vol/vol) O₂, and 75% (vol/vol) N₂. In this study, a peristaltic pump was used to circulate nanoparticles (20 μg mL⁻¹) in an M199 medium containing 2% FBS for the indicated time. The shear stress (τ) generated on the HUVECs was estimated as $6 Q \mu w^{-2}$, where Q is flow rate, w is the dimension in width, and μ is perfusate viscosity. The flow in the wide part was 12 dynes cm⁻². The MFI in this experiment was calculated from the plot profile of the whole image, the horizontal distance of the image every 50 μm was taken as an abscissa value, and the sum of the MFI every 50 μm was taken as an ordinate value to form a statistical curve.

Microfluidic Model of Vascular Stenosis: This model was adapted from Ingber et al.^[21] Microchannels mimicking vascular constriction were prepared from polydimethylsiloxane (PDMS) using conventional soft lithography. A master mold was prepared by aligning 80 μm layers designed using a computer-aided design program and formed using a cutter plotter (CE5000, Graphtec, CA). The device contained a region (160 μm in height × 400 μm in width × 10 mm in length) with a 90% constriction relative to upstream and downstream channel regions (each: 640 μm in height × 2 mm in width × 20 mm in length). The PDMS channels were sealed with glass using plasma bonding. In the study, MSNS or MSND solution (5 mL, 20 μg mL⁻¹) was recirculated through the microfluidic device using a syringe pump (LSP02-2A, LongerPump, China). The flow rate was adjusted to obtain a wall shear stress of 0.5 dyne cm⁻² (≈10 μL min⁻¹) at the unconstructed channels. For studies on the margination of nanoparticles to cells downstream of the stenotic regions, the microfluidic devices were sterilized using ethanol and UV irradiation and perfused with collagen I (50 μg mL⁻¹) to support cell adhesion. HUVECs were introduced to the microchannel and allowed to adhere under a static condition (4 h at 37 °C). The devices were then placed in a tissue culture incubator. A complete medium was infused (50 μL h⁻¹) using a syringe pump. For quantification, the number of RITC-labeled fluorescent spots in the field was counted, and data were shown by mean ± SEM from five independent experiments.

Real-Time Observation of Nanoparticle Margination in Mice: All animal studies were performed in accordance with the approved protocol of the Animal Care and Use Committee of Peking University and approved by the Ethics Committee of Peking University Health Science Center (LA2018155). Partial ligation of the mouse carotid artery to induce blood flow disturbance in the common carotid artery was performed as previously reported.^[51,52] Briefly, the left carotid bifurcation of mice was exposed following a neck incision. Three branches (external carotid, internal carotid, and occipital) of the left carotid artery were ligated with a 6-0 silk suture, and the superior thyroid artery was left unoperated. C57BL/6 wildtype mice were ligated or kept as sham controls (unligated) on the first day. On the second day, mice were anesthetized, and the carotid artery was exposed under a stereo fluorescence microscope (Stereo Discovery.V20, Zeiss). MSND or MSNS nanoparticles were intravenously injected. Movies were taken right after injection. The mice were observed in vivo for 30 min, and then the opening in the neck was closed and the mice were woken up.

En Face Analysis of Mice Aorta by Confocal Microscopy: C57BL/6 wildtype mice (12 weeks old, 22–25 g) were intravenously injected with MSNS or MSND nanoparticles (2 mg kg⁻¹). 24 h later, the mice were anesthetized and fixed with 4% PFA in PBS buffer for 10 min by perfusion through the left cardiac ventricle under physiological pressure. Aortas were harvested, further fixed with 4% PFA in PBS buffer for 20 min, and were then longitudinally dissected with microscissors. The luminal surfaces of the aortas were exposed, blocked with 3% bovine serum albumin in PBS for 1 h at room temperature, and were incubated with primary antibodies against VE-cadherin (Santa Cruz, 1:100) at 4 °C

overnight. The aortas were washed three times with PBS and were then probed with secondary antibodies including Alexa Fluor 488-conjugated goat anti-rabbit IgG (ThermoFisher, 1:500). Nuclei were counterstained with DAPI for 5 min at room temperature. Image acquisition was performed using laser-scanning confocal microscopy (Leica TCS SP8).

Biodistribution Study of MSND/MSNS in Mice: C57BL/6 mice were injected via the tail vein with RITC-labeled MSNS or MSND (2 mg kg⁻¹). 24 h later, the mice were sacrificed and perfused with 10 mL of PBS by injection through the left ventricle. The aorta, heart, liver, spleen, lung, and kidneys were dissected and then imaged by IVIS Spectrum (PE) ex vivo to obtain quantitative photon counts of their RITC intensities.

Drug Loading of Nanoparticles: According to a reported method,^[28] MSNS or MSND and DAC were added into 2 mL of PBS in a 10:1.5 ratio, and then stirred overnight in an icy water bath. Then, the solution was centrifuged for 20 min at 10000 rpm and the pellets were washed with PBS twice. DAC-loaded particles were resuspended with PBS and stored at -80 °C. The supernatant was collected, and absorbance at 240 nm was measured using a UV-vis spectrophotometer to calculate the DAC amount of supernatant. The drug loading efficiency (LE%) and encapsulation efficiency (EE%) are calculated as follows

$$EE\% = \frac{W_{\text{total}} - W_{\text{supernatant}}}{W_{\text{total}}} \quad (1)$$

$$LE\% = \frac{W_{\text{total}} - W_{\text{supernatant}}}{W_{\text{NP}} + W_{\text{total}} - W_{\text{supernatant}}} \quad (2)$$

where W_{total} represents the total amount of DAC, $W_{\text{supernatant}}$ represents the DAC amount of supernatant, and W_{NP} represents the weight of nanoparticles.

Assessment of In Vitro Drug Release: In vitro release of DAC was assessed in a PBS (pH 7.4) buffering system. DAC-loaded particles in PBS were transferred into dialysis bags (10 kDa weight cut-off). The dialysis bags were then put into PBS at 37 °C on a shaker at 90 rpm. 3 mL of solution was removed from the medium at different time points (0, 0.5, 1, 2, 4, 6, 8, 10, 12, 24, 36, 48, 60, and 72 h), and an equal amount of medium was added. The released DAC in the medium was measured by UV-vis spectrophotometer at 240 nm. Three biological replicates were performed.

Western Blotting: Cells were treated with PBS, DAC (2 μg mL⁻¹), MSNS, DAC-loaded MSNS, MSND, or DAC-loaded MSND (20 μg mL⁻¹) for 24 h. After that, the cells were homogenized in cold RIPA lysis buffer (25 mM HEPES, pH 7.4, 1% Triton X-100, 1% deoxycholate, 0.1% SDS, 125 mM NaCl, 5 mM EDTA, 50 mM NaF) supplemented with complete protease inhibitors cocktail. Equal amounts of cell lysates were separated on sodium dodecyl sulfate-polyacrylamide gel electrophoresis (SDS-PAGE), and then transferred to nitrocellulose membranes. Non-specific binding was blocked in 5% skim milk in Tris-buffered saline (TBS) containing 0.1% Tween-20. The membrane was incubated with specific primary antibodies overnight at 4 °C: DNMT1 (ABclonal, 1:1000), DNMT3A (ABclonal, 1:1000), DNMT3B (ABclonal, 1:1000), and GAPDH (Santa Cruz Biotech, 1:1000). Bound antibodies were detected by horseradish-peroxidase-conjugated secondary antibody and visualized by enhanced chemiluminescence.

Disturbed-Flow Accelerated Atherosclerosis Model: ApoE^{-/-} mice were obtained from the Experimental Animal Center at Peking University Health Science Center (Beijing, China). The mice were anesthetized and were then subjected to partial ligation of the carotid artery. Immediately after the surgery, the mice were fed on a high-cholesterol diet. One day later, the mice were subjected to PBS, DAC (0.2 mg kg⁻¹), MSNS, DAC-loaded MSNS, MSND, or DAC-loaded MSND (2 mg kg⁻¹) intravenously through the tail vein twice a week for 4 weeks. After that, the mice were sacrificed and fixed with 4% PFA in PBS for 10 min by perfusion through the left cardiac ventricle under physiological pressure. The ligated carotid arteries were harvested and subjected to histology and immunostaining analyses of atherosclerosis.

Hematoxylin and Eosin Staining: After rehydration, frozen sections were stained with hematoxylin solution for 20 s followed by 2 dips in 1% acid ethanol (1% HCl in 70% ethanol) and then rinsed in running water. Then, the sections were stained with eosin solution for 3 min

and followed by dehydration with graded alcohol (70%, 80%, 90%, 95%, 100%) and clearing in xylene.

Oil Red O Staining: Frozen sections were fixed in 4% PFA for 20 min and rinsed with PBS for 10 min and then rinsed with 60% isopropanol at room temperature. The sections were stained with Oil Red O (0.2% in 60% isopropanol) for 10 min with gentle shaking and rinsed again with 60% isopropanol and then with water three times. They were counterstain performed with Mayer's hematoxylin, washed, and sealed with glycogelatin. The plaque areas were determined using ImageJ software and calculated the average of three parts of the carotid artery by the plaque area relative to the total vascular area.

TUNEL Staining: Paraffin sections were deparaffinated, hydrated, and permeated. One Step TUNEL Apoptosis Assay Kit (MA0224, Meilunbio) was used according to the instructions. Terminal deoxynucleotidyl transferase (TdT) incorporation of tetramethylrhodamine-deoxyuridine triphosphate (TRITC-dUTP) into the 3'-hydroxyl terminal of the broken DNA of apoptotic cells. TRITC-dUTP-labeled DNA was observed directly by fluorescence microscopy (Leica DMI6000B; Leica TCS SP8).

Statistical Analysis: Data are presented as mean \pm SEM of the mean from at least three independent experiments as indicated. All analysis was performed using GraphPad Prism version 7.00. For in vitro experiments, the n value represents independent repeats or the number of cells or tests from at least three independent experiments. For in vivo experiments, the n value represents independent repeats or the number of animals. The normality of data distribution was tested with a D'Agostino–Pearson or Shapiro–Wilk test. For normally distributed data, differences between treatment groups were determined using unpaired t -test for two groups of data and one-way or two-way ANOVA or Brown–Forsythe and Welch ANOVA for multiple groups of data. Statistical significance among multiple groups was determined by post hoc analysis (Tukey honestly significant difference test). Nonparametric tests were used when data were not normally distributed, the Mann–Whitney test was used to examine the statistical significance between the two groups. Values of $p < 0.05$ were considered statistically significant.

Supporting Information

Supporting Information is available from the Wiley Online Library or from the author.

Acknowledgements

This work was funded by the National Natural Science Foundation of China (Projects 32201071 to C.Z.; 81974052, 82270419, and 81921001 to J.Z.; 82073773 to M.Y.; 82025032 to Y.G.), and the Ministry of Science and Technology (Project 2022YFC2704300 to J.Z.).

Conflict of Interest

The authors declare no conflict of interest.

Author Contributions

C.-R.Z., J.L., and Z.-T.J. contributed equally to this work. J.Z., Y.G., M.Y., and C.-R.Z. designed research, C.-R.Z., J.L., Z.-T.J., J.-J.Z., J.-N.Z., Q.-R.Y., and N.L. performed research. J.Z., Y.G., M.Y., C.-R.Z., and J.L. prepared the manuscript. J.-J.Z., Y.G., M.Y., C.-R.Z., J.L., Z.-T.J., W.Y., and W.P. analyzed the data. All authors carefully reviewed and approved the manuscript.

Data Availability Statement

The data that support the findings of this study are available from the corresponding author upon reasonable request.

Keywords

atherosclerosis, decitabine, endothelial inflammation, hemodynamics, nanoparticles

Received: July 31, 2022

Revised: October 22, 2022

Published online: November 20, 2022

- [1] J. S. Rana, S. S. Khan, D. M. Lloyd-Jones, S. Sidney, *J. Gen. Intern. Med.* **2021**, *36*, 2517.
- [2] J. J. Chiu, S. Chien, *Physiol. Rev.* **2011**, *91*, 327.
- [3] S. Chien, *Ann. Biomed. Eng.* **2008**, *36*, 554.
- [4] K. H. Ku, M. K. Dubinsky, A. N. Sukumar, N. Subramaniam, M. Y. M. Feasson, R. Nair, E. Tran, B. M. Steer, B. J. Knight, P. A. Marsden, *Circulation* **2021**, *144*, 365.
- [5] N. Niu, S. Xu, Y. Xu, P. J. Little, Z. G. Jin, *Trends Pharmacol. Sci.* **2019**, *40*, 253.
- [6] C. B. Fordyce, M. T. Roe, T. Ahmad, P. Libby, J. S. Borer, W. R. Hiatt, M. R. Bristow, M. Packer, S. M. Wasserman, N. Braunstein, B. Pitt, D. L. DeMets, K. Cooper-Arnold, P. W. Armstrong, S. D. Berkowitz, R. Scott, J. Prats, Z. S. Galis, N. Stockbridge, E. D. Peterson, R. M. Califf, *J. Am. Coll. Cardiol.* **2015**, *65*, 1567.
- [7] S. Zhang, Y. Liu, Y. Cao, S. Zhang, J. Sun, Y. Wang, S. Song, H. Zhang, *Adv. Mater.* **2022**, *34*, 2110660.
- [8] T. J. Beldman, T. S. Malinova, E. Desclos, A. E. Grootemaat, A. L. S. Misiak, S. van der Velden, C. van Roomen, L. Beckers, H. A. van Veen, P. M. Krawczyk, R. A. Hoebe, J. C. Sluimer, A. E. Neele, M. P. J. de Winther, N. N. van der Wel, E. Lutgens, W. J. M. Mulder, S. Huvneers, E. Kluza, *ACS Nano* **2019**, *13*, 13759.
- [9] L. Zhang, X. Y. Tian, C. K. W. Chan, Q. Bai, C. K. Cheng, F. M. Chen, M. S. H. Cheung, B. Yin, H. Yang, W. Y. Yung, Z. Chen, F. Ding, K. C. Leung, C. Zhang, Y. Huang, J. Y. W. Lau, C. H. J. Choi, *ACS Appl. Mater. Interfaces* **2019**, *11*, 13888.
- [10] C. Boada, A. Zinger, C. Tsao, P. Zhao, J. O. Martinez, K. Hartman, T. Naoi, R. Sukhoveshin, M. Sushnitha, R. Molinaro, B. Trachtenberg, J. P. Cooke, E. Tasciotti, *Circ. Res.* **2020**, *126*, 25.
- [11] B. R. Smith, S. S. Gambhir, *Chem. Rev.* **2017**, *117*, 901.
- [12] A. S. Gupta, *Wiley Interdiscip. Rev.: Nanomed. Nanobiotechnol.* **2016**, *8*, 255.
- [13] M. J. Mitchell, M. M. Billingsley, R. M. Haley, M. E. Wechsler, N. A. Peppas, R. Langer, *Nat. Rev. Drug Discovery* **2021**, *20*, 101.
- [14] S. Y. Lee, M. Ferrari, P. Decuzzi, *Nanotechnology* **2009**, *20*, 495101.
- [15] S. Shah, Y. Liu, W. Hu, J. Gao, *J. Nanosci. Nanotechnol.* **2011**, *11*, 919.
- [16] P. Decuzzi, M. Ferrari, *Biomaterials* **2006**, *27*, 5307.
- [17] L. H. Huang, J. Han, J. M. Ouyang, B. S. Gui, *J. Cell. Physiol.* **2020**, *235*, 465.
- [18] R. Agarwal, V. Singh, P. Journey, L. Shi, S. V. Sreenivasan, K. Roy, *Proc. Natl. Acad. Sci. USA* **2013**, *110*, 17247.
- [19] F. Gentile, C. Chiappini, D. Fine, R. C. Bhavane, M. S. Peluccio, M. M. Cheng, X. Liu, M. Ferrari, P. Decuzzi, *J. Biomech.* **2008**, *41*, 2312.
- [20] W. S. Nesbitt, E. Westein, F. J. Tovar-Lopez, E. Tolouei, A. Mitchell, J. Fu, J. Carberry, A. Fouras, S. P. Jackson, *Nat. Med.* **2009**, *15*, 665.
- [21] N. Korin, M. Kanapathipillai, B. D. Matthews, M. Crescente, A. Brill, T. Mammoto, K. Ghosh, S. Jurek, S. A. Bencherif, D. Bhatta, A. U. Coskun, C. L. Feldman, D. D. Wagner, D. E. Ingber, *Science* **2012**, *337*, 738.
- [22] Y. P. Zhang, Y. T. Huang, T. S. Huang, W. Pang, J. J. Zhu, Y. F. Liu, R. Z. Tang, C. R. Zhao, W. J. Yao, Y. S. Li, S. Chien, J. Zhou, *Sci. Rep.* **2017**, *7*, 14996.
- [23] J. Zhou, Y. S. Li, K. C. Wang, S. Chien, *Cell Mol. Bioeng.* **2014**, *7*, 218.

- [24] J. Dunn, H. Qiu, S. Kim, D. Jjingo, R. Hoffman, C. W. Kim, I. Jang, D. J. Son, D. Kim, C. Pan, Y. Fan, I. K. Jordan, H. Jo, *J. Clin. Invest.* **2014**, *124*, 3187.
- [25] J. F. Linnekamp, R. Butter, R. Spijker, J. P. Medema, H. W. M. van Laarhoven, *Cancer Treat. Rev.* **2017**, *54*, 10.
- [26] S. Landman, C. van der Horst, P. E. J. van Erp, I. Joosten, R. de Vries, H. Koenen, *J. Transl. Med.* **2021**, *19*, 11.
- [27] N. Hattori, M. Sako, K. Kimura, N. Iida, H. Takeshima, Y. Nakata, Y. Kono, T. Ushijima, *Clin. Epigenetics* **2019**, *11*, 111.
- [28] J. Cheng, Q. Ding, J. Wang, L. Deng, L. Yang, L. Tao, H. Lei, S. Lu, *Nanoscale* **2016**, *8*, 2011.
- [29] X. Wu, Z. Hu, S. Nizzero, G. Zhang, M. R. Ramirez, C. Shi, J. Zhou, M. Ferrari, H. Shen, *J. Controlled Release* **2017**, *268*, 92.
- [30] S. Y. Li, R. Sun, H. X. Wang, S. Shen, Y. Liu, X. J. Du, Y. H. Zhu, W. Jun, *J. Controlled Release* **2015**, *205*, 7.
- [31] A. Lesniak, A. Salvati, M. J. Santos-Martinez, M. W. Radomski, K. A. Dawson, C. Aberg, *J. Am. Chem. Soc.* **2013**, *135*, 1438.
- [32] T. Naganuma, *Nanoscale* **2017**, *9*, 13171.
- [33] G. Pyrgiotakis, C. O. Blattmann, P. Demokritou, *ACS Sustainable Chem. Eng.* **2014**, *2*, 1681.
- [34] J. J. Chiu, C. N. Chen, P. L. Lee, C. T. Yang, H. S. Chuang, S. Chien, S. Usami, *J. Biomech.* **2003**, *36*, 1883.
- [35] D. E. Conway, M. A. Schwartz, *J. Cell Sci.* **2013**, *126*, 5101.
- [36] X. Huang, G. Kong, Y. Li, W. Zhu, H. Xu, X. Zhang, J. Li, L. Wang, Z. Zhang, Y. Wu, X. Liu, X. Wang, *Biomed. Pharmacother.* **2016**, *84*, 447.
- [37] J. Yu, B. Qin, A. M. Moyer, S. Newshean, T. Liu, S. Qin, Y. Zhuang, D. Liu, S. W. Lu, K. R. Kalari, D. W. Visscher, J. A. Copland, S. A. McLaughlin, A. Moreno-Aspitia, D. W. Northfelt, R. J. Gray, Z. Lou, V. J. Suman, R. Weinshilboum, J. C. Boughey, M. P. Goetz, L. Wang, *J. Clin. Invest.* **2018**, *128*, 2376.
- [38] A. M. Flores, J. Ye, K. U. Jarr, N. Hosseini-Nassab, B. R. Smith, N. J. Leeper, *Arterioscler., Thromb., Vasc. Biol.* **2019**, *39*, 635.
- [39] A. G. Gilmartin, A. Groy, E. R. Gore, C. Atkins, E. R. Long, M. N. Montoute, Z. Wu, W. Halsey, D. E. McNulty, D. Ennulat, L. Rueda, M. Pappalardi, R. G. Kruger, M. T. McCabe, A. Raoof, R. Butlin, A. Stowell, M. Cockerill, I. Waddell, D. Ogilvie, J. Luengo, A. Jordan, A. B. Benowitz, *Haematologica* **2021**, *106*, 1979.
- [40] E. Westein, A. D. van der Meer, M. J. Kuijpers, J. P. Frimat, A. van den Berg, J. W. Heemskerk, *Proc. Natl. Acad. Sci. USA* **2013**, *110*, 1357.
- [41] S. Dasgupta, T. Auth, G. Gompfer, *Nano Lett.* **2014**, *14*, 687.
- [42] W. Zhang, Q. Li, C. Yang, H. Yang, J. Rao, X. Zhang, *Biochem. Biophys. Res. Commun.* **2020**, *524*, 70.
- [43] X. Qin, K. Zhang, J. Qiu, N. Wang, K. Qu, Y. Cui, J. Huang, L. Luo, Y. Zhong, T. Tian, W. Wu, Y. Wang, G. Wang, *Bioact. Mater.* **2022**, *9*, 397.
- [44] J. Kusunose, H. Zhang, M. K. Gagnon, T. Pan, S. I. Simon, K. W. Ferrara, *Ann. Biomed. Eng.* **2013**, *41*, 89.
- [45] K. Khodabandehlou, J. J. Masehi-Lano, C. Poon, J. Wang, E. J. Chung, *Exp. Biol. Med. (Maywood)* **2017**, *242*, 799.
- [46] A. J. Thompson, E. M. Mastroia, O. Eniola-Adefeso, *Biomaterials* **2013**, *34*, 5863.
- [47] A. C. Anselmo, C. L. Modery-Pawłowski, S. Menegatti, S. Kumar, D. R. Vogus, L. L. Tian, M. Chen, T. M. Squires, A. S. Gupta, S. Mitragotri, *ACS Nano* **2014**, *8*, 11243.
- [48] A. Da Silva-Candal, T. Brown, V. Krishnan, I. Lopez-Loureiro, A.-P. Gomez, A. Pusuluri, A. Perez-Diaz, C. Correa-Paz, P. Hervella, J. Castillo, S. Mitragotri, F. Campos, *J. Controlled Release* **2019**, *309*, 94.
- [49] P. Dogra, N. L. Adolphi, Z. Wang, Y. S. Lin, K. S. Butler, P. N. Durfee, J. G. Croissant, A. Noureddine, E. N. Coker, E. L. Bearer, V. Cristini, C. J. Brinker, *Nat. Commun.* **2018**, *9*, 4551.
- [50] X. Fang, C. Chen, Z. Liu, P. Liu, N. Zheng, *Nanoscale* **2011**, *3*, 1632.
- [51] C. R. Zhao, F. F. Yang, Q. Cui, D. Wang, Y. Zhou, Y. S. Li, Y. P. Zhang, R. Z. Tang, W. J. Yao, X. Wang, W. Pang, J. N. Zhao, Z. T. Jiang, J. J. Zhu, S. Chien, J. Zhou, *Proc. Natl. Acad. Sci. USA* **2021**, *118*.
- [52] D. Nam, C. W. Ni, A. Rezvan, J. Suo, K. Budzyn, A. Llanos, D. Harrison, D. Giddens, H. Jo, *Am. J. Physiol. Heart Circ. Physiol.* **2009**, *297*, H1535.